Exp Fluids (2011) 51:511–525
DOI 10.1007/s00348-011-1067-5

RESEARCH ARTICLE

Actuator disk model and span efficiency of flapping flight in bats based on time-resolved PIV measurements

Florian T. Muijres · Geoffrey R. Spedding · York Winter · Anders Hedenström

Received: 22 November 2010 / Accepted: 4 March 2011 / Published online: 23 March 2011
© Springer-Verlag 2011

Abstract All animals flap their wings in powered flight to provide both lift and thrust, yet few human-engineered designs do so. When combined with flexible wing surfaces, the resulting unsteady fluid flows and interactions in flapping flight can be complex to describe, understand, and model. Here, a simple modified actuator disk is used in a quasi-steady description of the net aerodynamic lift forces on several species of bat whose wakes are measured with time-resolved PIV. The model appears to capture the time-averaged and instantaneous lift forces on the wings and body, and could be used as basis for comparing flapping flight efficiency of different animal species and micro air vehicle designs.

1 Introduction

Flapping flight is often assumed to be more maneuverable compared to steady flight with fixed or constantly rotating wings, but evidence on transport efficiency (e.g. L/D_{max}) is more mixed. (Hall and Hall 1996; Hall et al. 1998; Wang 2008). A reduction in efficiency for flapping flight compared to steady wings is often explained using quasi-steady aerodynamic theory, where a steady wing can operate constantly at an optimal angle of attack, while a flapping wing needs to deviate from this optimum (Wang 2008). In a recent study, though Pesavento and Wang (2009) showed that for a 2D numerical model of a fruitfly wing, the flapping wing can be more efficient than the equivalent steady wing, due to unsteady wing-wake interactions at stroke reversal. Hall et al. (1998) use a viscous extension of the Betz criterion for optimal propellers to find the minimum power required for a flapping wing generating a prescribed lift and thrust. Due to a trade-off between efficient lift production and efficient thrust production, the flapping wing is slightly less efficient than an equivalent constant rotating wing (propeller).

Just a few human-engineered aircraft flap their wings to power flight, often being flapping micro air vehicles (MAVs, e.g. www.delfly.nl). Most flapping MAVs are inspired by flying animals, and also operate at Reynolds numbers (Re) similar to those of birds and bats ($10^3 \leq Re \leq 10^5$, $Re = Uc/\nu$, where U is the wing velocity, c is the mean chord length, and ν is the kinematic viscosity of air). In this Re range, the aerodynamics are hard to predict and control, because the laminar boundary layer on a wing can easily separate, and reattach after it has become turbulent (Lissaman 1983). This behavior is very sensitive to small changes in free-stream turbulence, ambient noise (Grundy et al. 2001) and wing geometry, and flexibility (Spedding et al. 2008).

Active flapping of biological or bio-inspired wings leads to further complications as the wing geometry changes can be significant fractions of the total wingbeat amplitude, and the deformations themselves are coupled with the time-

F. T. Muijres (✉) · A. Hedenström
Department of Biology, Lund University, Sölvegatan 37, SE-223 62 Lund, Sweden
e-mail: florian.muijres@teorekol.lu.se

G. R. Spedding
Department of Aerospace and Mechanical Engineering, University of Southern California, Los Angeles, CA 90089-1191, USA

Y. Winter
Cognitive Neurobiology, Humboldt University, Berlin, Germany

Y. Winter
NeuroCure Center of Excellence, Charité Universitätsmedizin Berlin, Dorotheenstrasse 94, 10117 Berlin, Germany

dependent aerodynamic forces. An example of a highly flexible flapping wing configuration is that of the bat, which has flexible membranous wings (Pennycuick 1971, 1973, 2008a; Swartz et al. 1996). When flapping, the wings deform continuously (Wolf et al. 2010; Swartz et al. 2007), under passive and active control (Hedenström et al. 2009). At slow flight speeds (at Strouhal number $St = 1.36$, $St = fA/U_\infty$, where f is the wing-beat frequency, A is the vertical flapping amplitude of the wing tip, and U_∞ is the forward flight speed), the Pallas' long-tongued bat (*Glossophaga soricina*) deforms and controls its wing in such a way that, during each downstroke, a leading edge vortex (LEV) is generated, which enhances lift during the downstroke by up to 40% of the total (Muijres et al. 2008).

This complex flow near the wing surface as well as the time-varying fluid–structure interactions are hard to measure and model, and so most aerodynamic measurements on flapping animal flight have focussed on far wake measurements (Spedding and Hedenström 2009). In the most common configuration, a three-dimensional model of the vortex wake of the flapping animals is assembled by identifying coherent vortex structures over a far wake domain that spans a streamwise distance equivalent to one wingbeat. By measuring the circulation of the various patches of vorticity the gross, time-averaged forces within a wingbeat can be estimated (Spedding et al. 2003a, b). This approach has improved our understanding of flapping animal flight significantly (Hedenström et al. 2006, 2007; Spedding et al. 2003a), but the 3D wake structure must be assembled by combining measurements from multiple wingbeats, with relatively poor resolution in the spanwise direction (normal to the plane of each slice). Moreover, the assemblage is constructed from only two velocity components, and the third, or its spatial gradient is inferred from vorticity conservation laws.

Recently, high speed stereo PIV systems have become available for animal flight research, with which the wake dynamics can be analyzed at a high temporal resolution (Hedenström et al. 2009; Hubel et al. 2009). In these studies, the wake is generally sampled using a transverse (vertical spanwise) PIV image at a typical frequency of 200 Hz. From the high-speed transverse PIV data, the three-dimensional vortex wake is assembled by identifying coherent streamwise vortex structures (Hubel et al. 2010), such as the tip vortex, from which the time varying flight forces can be estimated (Henningsson et al. 2010; Johansson and Hedenström 2009; Muijres et al. 2011). With these methods the temporal resolution is increased and the potential effect of the researcher's interpretation is reduced, resulting in more objective wake models. But since the forces generated by the flapping wing are typically modeled using tip vortex circulation, spanwise force distributions can not be determined.

A very simple model of flapping animal flight is the actuator disk (Ellington 1984; Norberg et al. 1993; Pennycuick 1968), which has originally been developed to estimate helicopter rotor performance (Gessow and Myers 1952). For this model, an actuator disk is defined as a circular surface with diameter equal to the wingspan, or alternatively equal to the width of the wake area behind the flying animal. These actuator disk models are very useful for estimating the average lift force and power for flapping flight, but can not be used for more detailed analysis since variations in induced velocities as a result of wingbeat kinematics are ignored.

In this study, we present a modified actuator disk model for forward flapping flight, which is adapted for use with near wake time-resolved PIV data of freely flying animals, using bats as a case in point. Here, the actuator disk area depends directly on the wake topology, and the measured induced downwash velocities within this modified disk are used to get a first-order estimate of the vertical impulse generated by the flapping wing both along the wingspan and throughout the wingbeat. From this the temporal lift force distribution is determined, as well as the induced power and the span efficiency factor. This approach enables us to estimate the performance of flapping flight at high spatial and temporal resolution, without having to model the fluid–structure interactions of the flexible wing, nor the highly unsteady fluid dynamics near the wing surface itself.

2 Methods

2.1 Experimental animals

Two bat species were studied, the Pallas' long-tongued bat (*Glossophaga soricina*, from here on called *G. soricina* and the lesser long-nosed bat (*Leptonycteris yerbabuenae*, from here on called *L. yerbabuenae*). Both species are small to medium sized new world nectar feeding bats of the subfamily *Glossophaginae*, and both are capable of hovering flight, which they habitually do when feeding from flowers. *L. yerbabuenae* is about twice the weight of *G. soricina* (Table 1), and is a migratory species, while *G. soricina* is a residential species. Of each bat species, a male and a female bat were used in the experiments. Relevant morphological data together with the estimated minimum power speed U_{mp} and maximum range speed U_{mr} (Norberg and Rayner 1987) for these bats are given in Table 1. Since U_{mp} and U_{mr} are similar for both bat species, we will directly compare the results for both species at the same flight speed.

In flapping flight, the airspeed that a flapping wing encounters is generally higher than the forward flight speed, due to the flapping motion of the wing. When

Table 1 Morphological data and typical flight speeds for the experimental bats

Bat (species, gender)	M (kg)	b (m)	S (m^2)	W/b (N/m)	U_{mp} (m/s)[a]	U_{mr} (m/s)[b]
G. soricina, male	0.0101	0.233	0.00879	0.425	3.26	5.09
G. soricina, female	0.0095	0.230	0.00860	0.405	3.27	5.01
L. yerbabuenae, male	0.0216	0.335	0.01576	0.633	3.70	5.39
L. yerbabuenae, female	0.0236	0.323	0.01529	0.717	3.67	5.56

The mass M was measured before and after each experiment. The wing span b, and wing surface area S were determined at mid downstroke, using the kinematics data. The span loading W/b is used to scale the induced power estimates. The minimum power speed U_{mp}, and maximum range speed U_{mr} are estimated from the morphological data following Norberg and Rayner (1987)

[a] $U_{mp} = 6.58\ M^{0.422}\ b^{-0.479}\ S^{-0.148}$

[b] $U_{mr} = 8.71\ M^{0.423}\ b^{-0.498}\ S^{-0.144}$

assuming a sinusoidal flapping motion, this average effective free-stream speed $\left(U_{\infty,\mathrm{eff}}\right)$ can be estimated by (e.g. Lentink and Gerritsma 2003)

$$U_{\infty,\mathrm{eff}} = U_{\infty}\sqrt{St^2 + 1}. \quad (1)$$

$U_{\infty,\mathrm{eff}}$ is based on the forward flight speed and the flapping motion of the wing, but any induced fluid motion is ignored, hence the addition of 'free-stream'. For *G. soricina* St can be estimated by $St \approx 1.26\ U_{\infty}^{-0.85}$ (Wolf et al. 2010), while, for *L. yerbabuenae* it may be approximated by $St \approx 1.28\ U_{\infty}^{-0.90}$ (R. von Busse, L.C. Johansson, Y. Winter and A. Hedenström, unpublished data). We will use the effective free-stream velocity $U_{\infty,\mathrm{eff}}$, instead of the commonly used U_{∞}, as the general velocity scaling parameter (e.g. for Re and C_L). At the flight speeds range studied ($2\ \mathrm{m/s} < U_{\infty} < 7\ \mathrm{m/s}$), the Reynolds number range based on $U_{\infty,\mathrm{eff}}$ and c is in the order of $1 \times 10^4 < Re_{\mathrm{eff}} < 2{\cdot}10^4$ for both bat species. This is a similar range to local effective Reynolds numbers of wings of small birds (Rosén et al. 2007).

2.2 Experimental setup

Experiments were performed in the Lund University low-turbulence, low-speed wind tunnel (Pennycuick et al. 1997, Fig. 1). The experimental setup used in this study is the same as described in Hedenström et al. (2009), where preliminary data for this study were presented. The bats were trained to fly in front of a feeder in the test section of the wind tunnel, at a speed ranging from $U_{\infty} = 2$ m/s to 7 m/s, in increments of 1 m/s, with an extra step at 2.5 m/s. 20 cm downstream from the feeder a 20×20 cm^2 PIV image plane was positioned, resulting in an average distance between the trailing edge of the bat wing and the image plane of approximately 10 cm (2–3 c, Fig. 1). A rectangular coordinate system is defined with x running in the streamwise direction, y the spanwise direction and z is positive opposing the direction of gravitational acceleration, $\{u, v, w\}$ are the velocity components in these

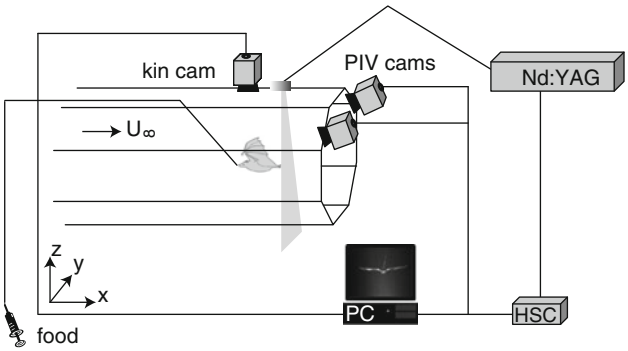

Fig. 1 The experimental setup consists of a high-speed stereo PIV setup, synchronized with a top view high-speed kinematics camera in a wind tunnel. The position of the bat is controlled using a manually operated feeder system

directions. The origin of the coordinate system is at the PIV image plane, directly downstream from the feeder. The high-speed stereo PIV system consisted of a transverse laser sheet (aligned in the y–z plane), generated by a 200 Hz pulsed 50 mJ Laser (Litron LPY732 series, Nd:YAG, 532 nm), and two CMOS-cameras (HighSpeedStar3; 1,024 × 1,024 pixels). The system was controlled using DaVis software (LaVision 7.2.2.110).

For the experiments, the wind tunnel was set to the required forward flight speed, while the bats were roosting in the settling chamber. When a bat wanted to eat, it flew with the wind downstream into the test section, made a U-turn and approached the feeder from downstream. While the bat was judged to be flying steadily at the feeder, a sequence of 50 frame pairs were acquired at a sample rate of 200 Hz. The ¼ s period is equal to three to four wingbeats. The time separation between PIV frames (δt) was set so mean pixel displacements in the wake of the bat were in the order of 3.5, and not close to an integer value to reduce peak locking. It ranged from $\delta t \approx 200$ µs at 2 m/s to $\delta t \approx 100$ µs at 7 m/s.

Simultaneously with the PIV recording, the bat was filmed from above with a NAC HotShot 1280 video camera, (640 × 512 pixels, 250 Hz sampling rate and shutter

speed 1/250 s, Fig. 1). The video sequences were used to identify the individual and to determine the bat's position, attitude, basic wing kinematics, and morphological data.

2.3 Analysis

The PIV images were analyzed using Davis (Lavision 7.2.2.110), as described in (Hedenström et al. 2009). A multi-pass stereo cross-correlation (64 × 64, 32 × 32, 50% overlap) was used, and the data were post-processed using a 3 × 3 smoothing average, resulting in an inplane spatial resolution of the velocity vectors of 5.1 mm. The resulting velocity fields were interrogated using a custom Matlab (7.7.0.471, R2008b) program where the velocity components $\{u, v, w\}$ at the image plane location $\{y, z\}$ were extracted on specified transects and stored.

For each PIV sequence, the frames within one wingbeat were given a frame number $n = [1{-}N]$, a non-dimensional time stamp $\tau = [0{-}1]$ and a streamwise position $x = [0{-}\lambda]$, where λ is the wavelength of the wingbeat. The start ($n = 1$) and end frames ($n = N$) coincide with the part of the wake generated by the start of the downstroke. The non-dimensional time stamp is defined as $\tau = t/T$, where T is the wingbeat period, and t is the moment at which the wake structure measured in PIV frame n is generated by the flapping wing, $t = 0$ is equivalent to the start of the downstroke, and $t = T$ is the end of the upstroke. Since the flapping bat wings travel forward with respect to the PIV image plane during the downstroke, and backwards during the upstroke, a Doppler shift is present in the PIV data, resulting in an overrepresentation of the downstroke in the PIV frames. By assuming that the wing moves forward and backwards at a constant speed, the non-dimensional time stamp for PIV frame n are determined by

$$\begin{aligned} \tau &= \frac{(n-1)}{N}\frac{t_{\text{ds wing}}}{t_{\text{ds wake}}} \text{ for } 1 \le n \le N_{\text{du}} \\ \tau &= \frac{(n-1)}{N}\frac{t_{\text{us wing}}}{t_{\text{us wake}}} \text{ for } N_{\text{du}} \le n \le N \end{aligned} \tag{3}$$

where N_{du} is the PIV frame at the transition from downstroke to upstroke. $t_{\text{ds wing}}/t_{\text{ds wake}}$ is the ratio between the downstroke duration of the wing and the downstroke duration of the PIV sequence, and $t_{\text{us wing}}/t_{\text{us wake}}$ is the ratio between the upstroke duration of the wing and the upstroke duration of the PIV sequence.

If we assume that the wake convects statically downstream with the forward flight speed U_∞, the streamwise position for PIV frame n is

$$x = (n-1)\, U_\infty \cdot \Delta t \tag{4}$$

where Δt is the inverse of the PIV frame rate ($\Delta t =$ 1/200 s). Using these x-values, the three-dimensional wake field behind the flying animal can be constructed. Each node-point within the resulting three-dimensional wake matrix consists of a position vector $\{x, y, z\}$ and the three velocity components $\{u, v, w\}$. The resolution of the wake field is, in y-and z-direction, equal to the PIV vector node point spacing $\Delta y = 5.1$ mm, and in x-direction equal to $\Delta x = U_\infty \cdot \Delta t$, which will vary from $\Delta x = 10.0$ mm at $U_\infty = 2$ m/s to $\Delta x = 35.0$ mm at $U_\infty = 7$ m/s. To compensate for the low resolution in x-direction a cubic interpolation routine is used (Matlab, interp3), resulting in a streamwise resolution in the interpolated wake matrix of 5 mm for all flight speeds. For this interpolated wake matrix the vorticity magnitude $\left(|\omega| = \sqrt{\omega_x^2 + \omega_y^2 + \omega_z^2}\right)$ is calculated. Controlled tests on an artificial vortex tube of similar strength and size as for the bats, oriented in y-direction, showed that at the highest flight speeds, the interpolation routine still results in an underestimation of ω_y (e.g. vorticity of start or stop vortices).

3 The actuator disk model for flapping flight

The actuator disk model (Gessow and Myers 1952; Spalart 2003; Stepniewski and Keys 1984) is a highly simplified model for force and power estimations of constantly rotating wings, originally developed for helicopter rotors, but also adapted for flapping animal flight (Pennycuick 2008b). The basic model defines the actuator disk as a circular disk swept by the wing configuration, typically a rotor or a propeller.

Let us first assume an ideal rotor during forward flight (Fig. 2a). Due to wing rotation, a uniform pressure difference (Δp) is created across the propeller disk, resulting in an induced airflow with velocity vector $\bar{u} = \{u, w\}$ at the disk surface. For an ideal actuator disk the induced velocity $\bar{u}$ is often assumed to be uniform throughout the disk area, although Spalart (2003) showed that this assumption is incorrect, even for a uniform Δp. The induced velocities far upstream of the disk are zero ($\bar{u}_0 = 0$, Fig. 2a), while the induced velocities attained in the far wake $\bar{u}_\infty = \{u_\infty, w_\infty\}$ are twice the induced velocity at the disk ($\bar{u}_\infty = 2\bar{u}$). If we ignore the streamwise component of the induced velocity vector ($\bar{u} \approx \{w\}$), the lift force L and induced (or shaft) power generated by the propeller can be estimated as

$$\begin{aligned} L &= -2\,\dot{m}\,w \\ P_{i\,\text{ideal}} &= -L\,w \end{aligned} \tag{5}$$

where $\dot{m}$ is the mass flux through the disk, defined as

$$\dot{m} = \rho\, A_d\, |\bar{U}_d| \tag{6}$$

where ρ is the air density, A_d is the disk area, and $\bar{U}_d = \{U_\infty, w\}$ is the total velocity vector at the disk. There is a minus sign in Eq. 5 since a downwash (negative w) will

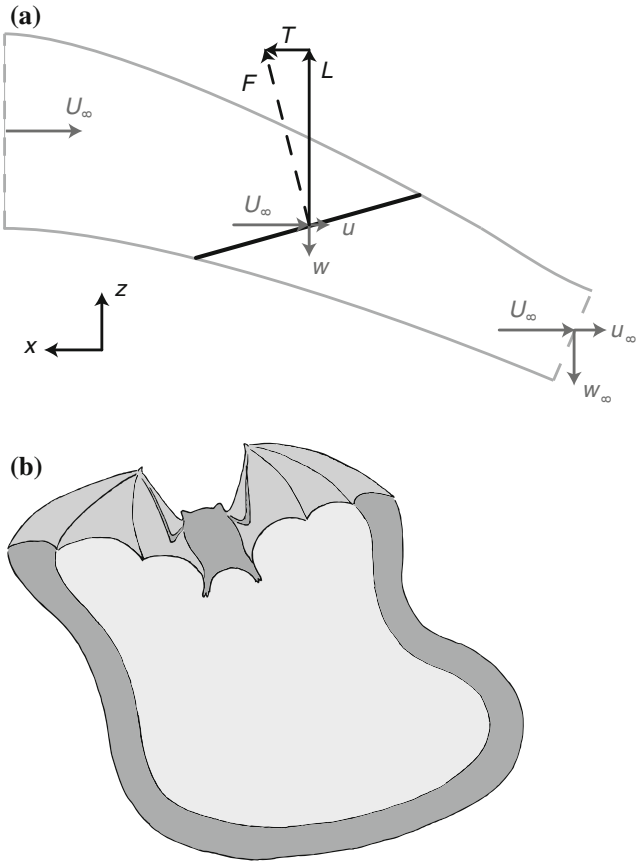

Fig. 2 **a** An ideal actuator disk in forward flight. A uniform pressure difference generated by the rotating disk causes air to accelerate through the disk. This results in an induced velocity change from $\bar{u}_0 = 0$ far upstream to $\bar{u}_\infty = 2\,\bar{u}$ far downstream, and a flight force production F with lift component L and thrust component T. **b** Cartoon illustration of a flying bat with its actuator disk wake. The disk area is bound by the main vortex structures (start vortex, tip vortices, and stop vortex). In this image, the stop vortex has not yet been shed

result in a positive lift, and the factor 2 is due to the fact that $w_\infty = 2w$. $P_{i\,\mathrm{ideal}}$ is called the ideal induced power, since it is the power required for generating a uniform downwash within the actuator disk area, and this uniform downwash is the lowest energy solution for a given momentum flux (Stepniewski and Keys 1984).

This general actuator disk model for forward flight has been applied to animal flight (Pennycuick 1968), by defining the actuator disk of the flapping wings as a circular area with the diameter equal to the wing span, and the forces and induced power for a flying animal can directly be determined using the above described theory. This highly simplified model for flapping flight of animals can be used to determine the required power for flight and for estimating the average flight forces throughout a wingbeat, but it cannot be used for more detailed studies, such as for estimating temporal or spatial force distributions within a wingbeat.

Here, we propose a modified area for the actuator disk, which is directly based on the wake area generated by the flapping wing configuration, and which enables us to study the aerodynamics of flapping flight in more detail. Our modified actuator disk area for flapping flight is defined as the area spanned by the main vortex structures generated within one wingbeat (start, stop and tip vortices, Fig. 2b). The area can be constructed from the PIV data, by tracing the area between the two tip vortices for all PIV frames within one wing beat (PIV frame $n = [1{-}N]$). Throughout the modified actuator disk area, the vertical induced velocity is not assumed to be uniform, but is measured. This downwash variation can be used to analyze flapping flight in detail. The variations in streamwise direction (x-direction) can be used to estimate the relative contribution of various parts of the wingbeat, e.g. lift generated by the downstroke versus lift generated by the upstroke. The downwash variation in spanwise direction (y-direction) can be used to determine the real induced power P_i and the span efficiency e_i, as described below. Equations 5 and 6 are converted to implement the variation of w throughout the actuator disk as follows

$$\dot{m} = \rho \cdot A_d \cdot w = \rho \int_0^{\lambda} \int_{-b_w(x)/2}^{b_w(x)/2} w(x,y)\mathrm{d}y\mathrm{d}x$$

$$L = -2\dot{m}_z\, w = -2 \int_0^{\lambda} \int_{-b_w(x)/2}^{b_w(x)/2} \dot{m}_z(x,y) w(x,y)\mathrm{d}y\mathrm{d}x \qquad (7)$$

$$P_i = -Lw = -\int_0^{\lambda} \int_{-b_w(x)/2}^{b_w(x)/2} L(x,y) w(x,y)\mathrm{d}y\mathrm{d}x$$

where λ is the wavelength of the flapping wing motion defined as $\lambda = U_\infty/f$, which is equal to the extent of the actuator disk in streamwise direction (along x-axis). Thus, the U_∞ component in the mass flux estimate is incorporated into the disk area as λ. $b_w(x)$ is the wake width, which varies throughout the wingbeat as a result of the varying wing span due to the flapping motion. Since the downwash is not assumed uniform throughout the actuator disk in Eq. 7, the real induced power (P_i) is calculated rather than $P_{i\ \mathrm{ideal}}$.

Note that the actuator disk model estimates only the (vertical) lift production and corresponding induced power. The thrust component of the flight forces are ignored, since we cannot distinguish streamwise induced velocities as a result of thrust production from wake defects due to drag, and since thrust forces are small compared to lift forces for these bats (Muijres et al. 2011).

If we assume that the downwash along the wingspan at streamwise location x, depends directly and solely on the

instantaneously generated lift at the corresponding subsection of the wingbeat, the mass flux, lift and induced power per distance travelled are

$$\dot{m}'_z(x) = \rho \int_{-b_w(x)/2}^{b_w(x)/2} w(x,y)\mathrm{d}y$$
$$L'(x) = -2 \int_{-b_w(x)/2}^{b_w(x)/2} \dot{m}_z(x,y)w(x,y)\mathrm{d}y \quad (8)$$
$$P'_i(x) = -\int_{-b_w(x)/2}^{b_w(x)/2} L(x,y)w(x,y)\mathrm{d}y$$

To be able to estimate the corresponding ideal induced power per distance travelled, we first need to determine the spanwise uniform vertical induced velocity ($\bar{w}(x)$) which would result in $L'(x)$ by

$$\bar{w}(x) = -\sqrt{\frac{L'(x)}{2\rho b_w(x)}}. \quad (9)$$

The ideal induced power per distance travelled can now be estimated by

$$P'_{i\,\mathrm{ideal}}(x) = -L'(x)\bar{w}(x). \quad (10)$$

This is the minimum required power per distance travelled to generate $L'(x)$, and which would be a result of an elliptical spanwise lift distribution (Anderson 1991; Spedding and McArthur 2010). The total ideal power for the whole wingbeat can be determined by integrating along the complete wingbeat (x-axis)

$$P_{i\,\mathrm{ideal}} = -\int_0^{\lambda} P'_{i\,\mathrm{ideal}}(x)\mathrm{d}x = \int_0^{\lambda} L'(x)\bar{w}(x)\mathrm{d}x. \quad (11)$$

This estimate of $P_{i\,\mathrm{ideal}}$ will be higher than for Eq. 5, because in Eq. 5 the downwash is assumed to be uniform throughout the complete actuator disk, while for Eq. 11 the downwash is assumed uniform only along the wingspan ($\bar{w}(x)$), and can vary throughout the wingbeat. The ratio between $P_{i\,\mathrm{ideal}}$ and P_i is called the span efficiency, and it is a direct estimate of efficiency reduction due to a deviation from a spanwise uniform downwash distribution (Spedding and McArthur 2010), for a complete wingbeat in forward flapping flight. Therefore, we will use the corresponding span efficiency notation proposed by Spedding and McArthur (2010), where e_i is the span efficiency due to downwash distribution only

$$e_i = \frac{P_{i\,\mathrm{ideal}}}{P_i}. \quad (12)$$

For isolated wings in steady, horizontal flight where L balances W, the induced power can be estimated from

$$P_i = D_i U_\infty = \left(\frac{W}{b}\right)^2 \frac{2}{\pi\rho U_\infty}\frac{1}{e_i} \quad (13)$$

where D_i is the induced drag, W is the weight of the flapping configuration, and b is the wing span. So, we will assume that the here estimated real induced power should scale with span loading squared $(W/b)^2$, the inverse flight speed $(1/U_\infty)$, and the inverse span efficiency $(1/e_i)$.

4 Analysis

The above described actuator disk model for forward flapping flight will be used to analyze transverse PIV results of the wake of two bat species flying steadily in a wind tunnel. Figure 3 shows such PIV data for both species flying at 4 m/s. Throughout almost the complete wingbeat (Fig. 3a–c, e–g), the tip-vortex is present as the large blue patch of negative vorticity (center marked with a grey dot), inducing a downwash behind the wing (between the tip-vortex and the position behind the body). For both bat species, the tip-vortex has changed sign (yellow/orange patch of positive vorticity) at the end of the upstroke (Fig. 3d, h), resulting in an upwash (negative lift) behind the outer wing. The "vortices" in Fig. 3 are simply compact, contiguous patches of high vorticity magnitude, that for convenience are described as vortices in the remainder of this paper.

The local shape and orientation of the actuator disk at each PIV frame is defined as a straight line from the center of the tip-vortex to the position behind the body (red lines in Fig. 3). The actuator disk line for PIV frame n is called actuator disk segment n with local semi-span $b_w(n)/2$. By mirroring the results along the z-axis at the body centerline, the complete local actuator disk segment n with local span $b_w(n)$ is defined. By adding the actuator disk segments for all PIV frames within one wingbeat, and using the x-variable for each PIV frame for the streamwise distribution, the actuator disk for the complete wingbeat is defined.

Each PIV vector node point along an actuator disk segment n is marked using an index m along the spanwise y-axis, and the vertical induced velocity at each node point $w_\mathrm{PIV}(n, m)$ is used as input for the actuator disk model calculations. Since the PIV image plane is positioned downstream of the bat, the measured downwash velocities $w_\mathrm{PIV}(n, m)$ will be higher than at the actuator disk (in this case at the bat wing, Fig. 4a), but since the distance between wing and PIV plane is small (2–3 c) we can assume that these differences are small, and we will assume $w_\mathrm{PIV} = w$. One could argue that far wake measurements (where $w \approx w_\infty$) would avoid this uncertainty, but we can assume that spanwise downwash distributions in the far wake would deviate significantly from that at the wing due to wake interactions (Johansson et al. 2008).

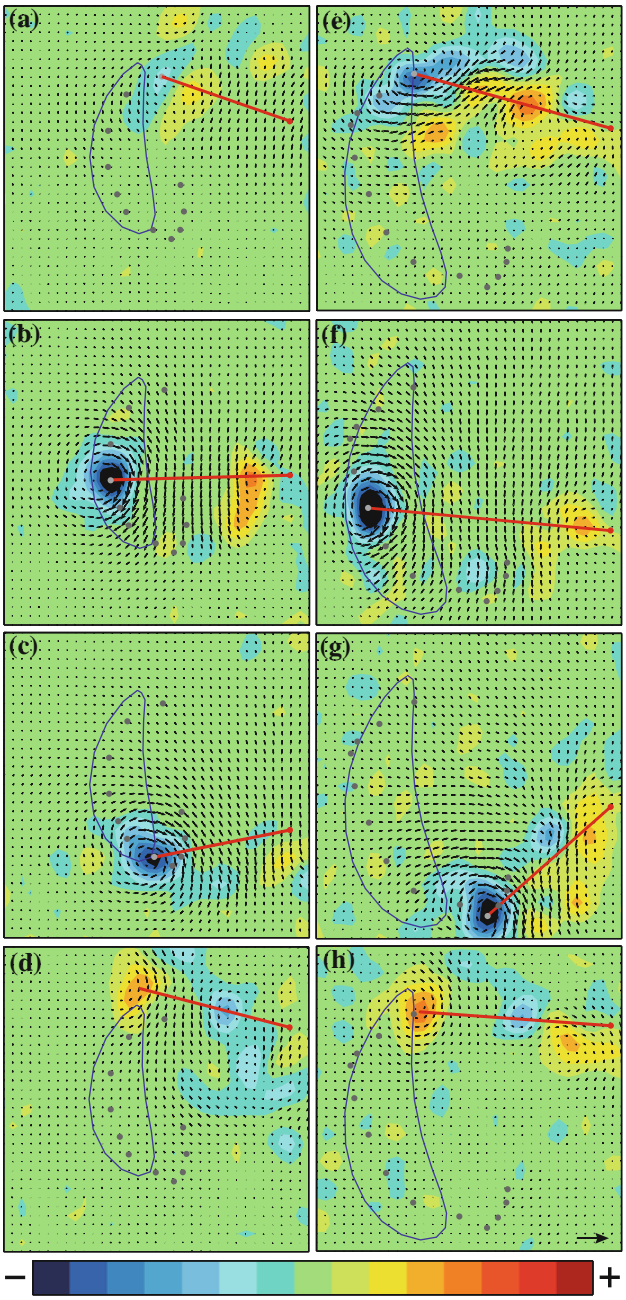

Fig. 3 Transverse PIV results for one wingbeat of both bat species flying at 4 m/s. The left panels (**a**–**d**) show the results for *G. soricina*, while the right panels (**e**–**h**) show the results for *L. yerbabuenae*, at the start of the downstroke (**a**, **e**); mid-downstroke (**b**, **f**); end of the downstroke (**c**, **g**); end of the upstroke (**d**, **h**). The *arrows* are the inplane velocity vectors, scaled with the reference vector of 5 m/s in panel (**h**). The colors visualize the streamwise vorticity ω_x, scaled according to the scale bar on the bottom of the figure, with range $-300 < \omega_x < 300$. The grey dots show the tip vortex location in the different PIV frames n, with the *light grey* dot indicating the current frame, while the *blue line* shows the wingtip movement throughout the wingbeat

For each individual bat and flight speed combination, at least 5 flight sequences were analyzed, which consisted on average of 11 wingbeats. From the wake data for each species and flight speed combination a single average actuator disk was determined, resulting in an average wake based on at least 20 wingbeats. The average actuator disk is constructed by dividing the actuator disk in streamwise direction into $\bar{N}$ elements, where $\bar{N}$ is the mean number of PIV frames per wingbeat for the analyzed wingbeats. Within each element ($\bar{n} = [1 - \bar{N}]$), the average spanwise downwash distribution was determined by fitting a cubic smoothing spline (Matlab, csaps, smoothing parameter = 1–10^{-4}) through the $w(\bar{n}, m)$ datapoint distribution (Fig. 4b). The relative deviation of the $w(\bar{n}, m)$ node points from the average spline were estimated using a sliding 95% confidence interval (Fig. 4b), determined from a sliding window of 20 local data points (which is equal to the minimum amount of wingbeats used to determine the average actuator disk).

The resulting spline function for each segment $\bar{n}$ was directly used to determine the lift and power contribution using Eqs. 8–11. The actuator disk's total lift and total induced power was determined by summing the $\bar{N}$ elements

$$L = \Delta x \sum_{\bar{n}=1}^{\bar{N}} L'(\bar{n})$$

$$P_i = \Delta x \sum_{\bar{n}=1}^{\bar{N}} P_i'(\bar{n}). \qquad (14)$$

$$P_{i\,\mathrm{ideal}} = \Delta x \sum_{\bar{n}=1}^{\bar{N}} P'_{i\,\mathrm{ideal}}(\bar{n})$$

The effective span efficiency e_i for each average wingbeat was determined from $P_{i\ \mathrm{ideal}}$ and P_i using Eq. 12.

To test how the lift, power and span efficiencies vary with flight speed and between the two bat species we used mixed linear models. Since the bats fly steadily at the feeder, the total lift should be equal to the weight of the animals. Therefore, L is non-dimensionalized as L/W, and $L/W-1$ is set as the dependent variable in the mixed linear model, for each species separately. U_∞ is set as a covariate. To control for differences in P_i due to differences in span loading between the individuals (Eq. 13), $P_i(b/W)^2$ is set as the dependent variable in the mixed linear model. Since $P_i(b/W)^2$ should scale with $1/U_\infty$ (Eq. 13), $1/U_\infty$, *species*, and "$1/U_\infty$ X *species*" are set as covariates. For the span efficiency test e_i is set as the dependent variable, and *species*, U_∞ and interaction between *species* and U_∞ are used as covariates.

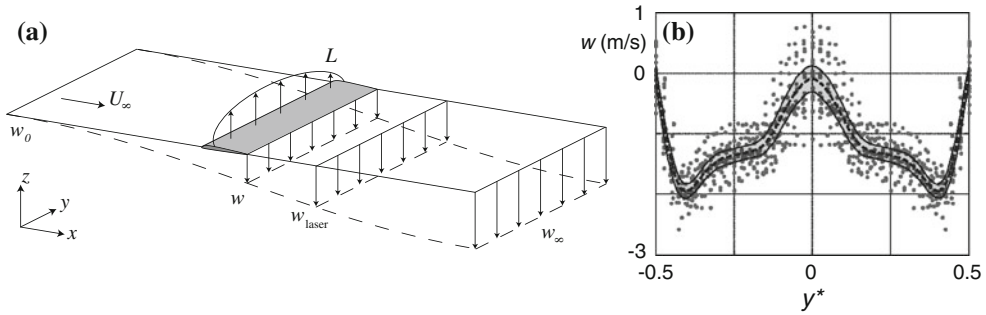

Fig. 4 **a** The vertical induced velocity behind a steady wing with an elliptical lift-distribution *L*. The downwash increases from $w_0 = 0$ far upstream, to $w_\infty = 2w$ far downstream in the wake. At the PIV laser location, we assume $w_{PIV} = w$. **b** The vertical induced velocity distribution $w(y^*)$ along the non-dimensionalized wake span $y^* = y/b_w$ at mid downstroke, for *G. soricina* at 4 m/s. The datapoints are determined from the PIV data of 20 analyzed wingbeats, the *dotted line* is the smoothing spline through these data, and the *shaded area* around the *dotted line* shows the 95% confidence interval

5 Results

5.1 Wake topology and actuator disk area

Actuator disks constructed using the PIV data for *G. soricina* at three flight speeds are shown in Fig. 5 as the multicolored surfaces spanned between the wake vortices. The vortex wake is visualized using green iso-surfaces of constant absolute vorticity $|\omega|$ in the three-dimensional interpolated wake field $\{x, y, z\}$. The actuator disk surface spanned between the main vortices is color-coded using the vertical induced velocity strength.

The vorticity magnitude iso-surfaces confirm previous wake structure descriptions for bats (Hedenström et al. 2007; Hubel et al. 2010; Muijres et al. 2011), but unrestricted from having only the streamwise vorticity component. At the lowest flight speed ($U_\infty = 2$ m/s, Fig. 5a), a start vortex is generated by each wing at the beginning of the downstroke. Each start vortex connects to the tip-vortex and a vortex which is probably shed from the root of the wing. Therefore, this vortex is called the root vortex (Hedenström et al. 2007; Muijres et al. 2011). Between each tip- and root vortex, so behind the outer wing, the downwash is largest (see actuator disk surfaces in Fig. 5a), while between the root vortices (behind the body) hardly any downwash is present. Both the tip and root vortices are present throughout the whole downstroke, but their strength drops below the iso-surface threshold at the start of the upstroke. During the upstroke no strong vortex structure is present, indicating that the upstroke is relatively inactive at 2 m/s.

At the medium flight speed ($U_\infty = 4$ m/s, Fig. 5b), the vortex structure during the downstroke is very similar to that at $U_\infty = 2$ m/s, while during the upstroke, the wake is very different from that at $U_\infty = 2$ m/s. During the first part of the upstroke the tip vortices are still present at 4 m/s. They disappear at the second half of the upstroke, after which two small vortex loops appear, one behind each wing, resulting in an upwash at this part of the wake. Since these vortex loops generate an upwash, resulting in negative lift, they are denoted as reversed vortex loops. Reversed vortex dipoles were also noted by Hedenström et al. (2007), Johansson et al. (2008), Hubel et al. (2010) and Muijres et al. (2011), but here we can confirm that each reversed vortex dipole is in fact part of a vortex loop.

At the highest flight speed ($U_\infty = 7$ m/s, Fig. 5c) the same wake structures are present as at 4 m/s, but the relative strength of the structures are different. At $U_\infty = 7$ m/s, the root vortices are present throughout almost the complete wingbeat, resulting in a reduction in downwash behind the body, also during the upstroke. The reversed vortex loops are stretched out along a large part of the wingbeat, resulting in more upwash and more negative lift. The start vortices and the spanwise part of the reversed vortex loops are not visible in Fig. 5c, which could be because the spanwise vorticity ω_y is underestimated, or because the spanwise vortices are stretched out in streamwise direction due to the higher flight speed (Johansson et al. 2008), resulting in maximum vorticity values below the iso-surface threshold.

5.2 Wingbeat average lift production

The overall uncertainty of the actuator disk model for forward flapping flight was estimated by comparing the calculated lift with the known weight of the bats. The lift-to-weight ratio, *L*/*W*, for *G. soricina* is not significantly different from one ($L/W = 0.98 \pm 0.10$, mean $\pm$ SD), but for *L. yerbabuenae* it is ($L/W = 0.87 \pm 0.13$), as is the variation with speed (Table 2 and Fig. 6a). Figure 6b shows the average lift-coefficient, C_L, throughout the wingbeat for the same data as in Fig. 6a, defined as

$$C_L = \frac{L}{1/2\rho U_{\infty,\mathrm{eff}}{}^2 S}. \quad (15)$$

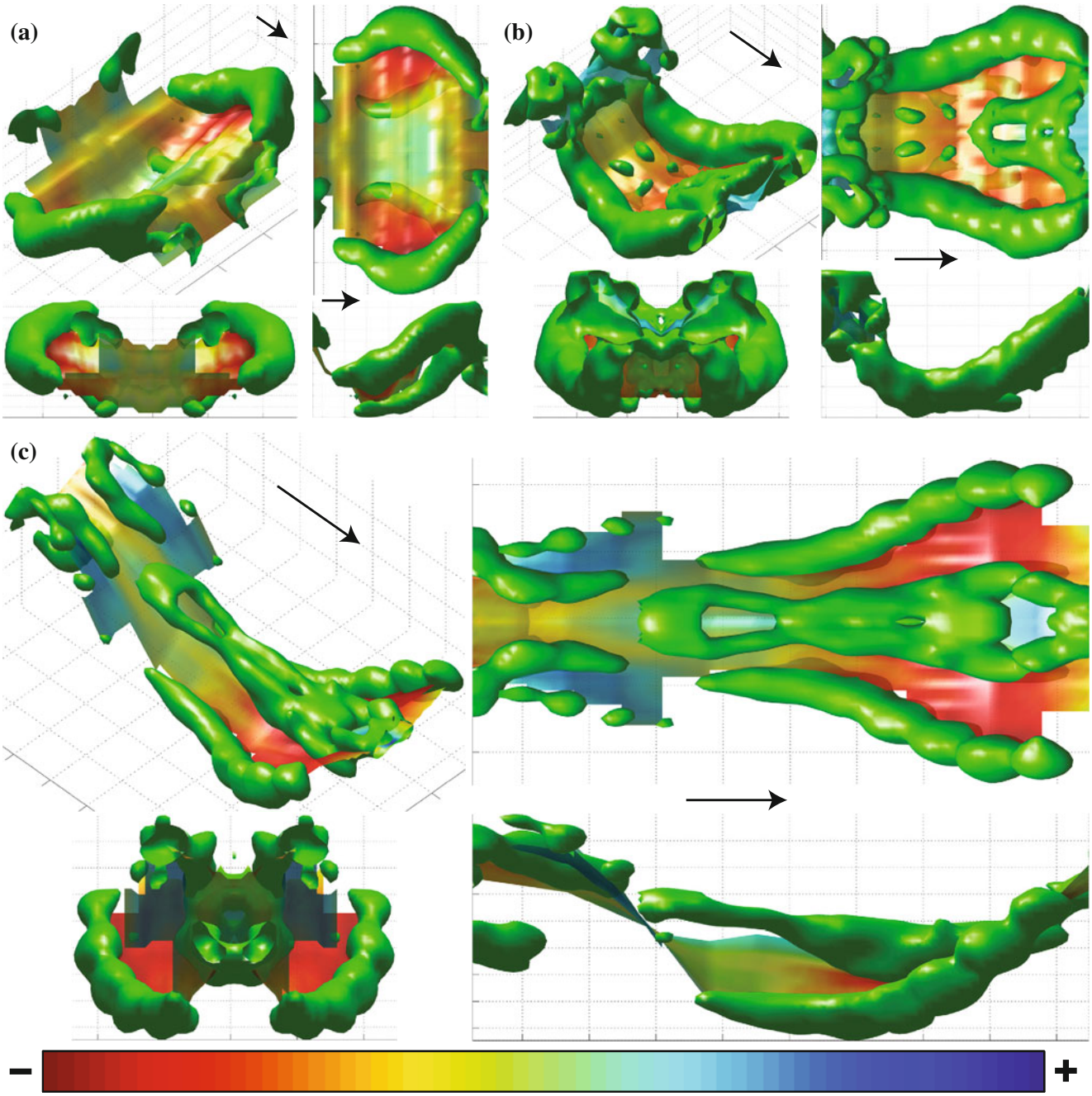

Fig. 5 Vortex-wake and actuator disk surface for a single wingbeat of *G. soricina* flying at different flight speeds. The vortex wake is visualized using green iso-surfaces of constant absolute vorticity $|\omega|$. The actuator disk surface encircled by the vortex structures is color-coded using the vertical induced velocity w according to the color bar on the bottom of the figure. The different panels show the wake at (**a**) $U_\infty = 2$ m/s, with iso-value $|\omega|_{\text{iso}} = 200\ \text{s}^{-1}$, and color bar range $-2.6\ \text{m/s} < w < 2.6\ \text{m/s}$; (**b**) $U_\infty = 4$ m/s, $|\omega|_{\text{iso}} = 125\ \text{s}^{-1}$, $-2.6\ \text{m/s} < w < 2.6\ \text{m/s}$; and (**c**) $U_\infty = 7$ m/s, $|\omega|_{\text{iso}} = 125\ \text{s}^{-1}$, $-1.7\ \text{m/s} < w < 1.7\ \text{m/s}$. Each panel consists of 4 different views: (NW) perspective view; (NE) top view; (SW) front (upstream) view; (SW) side view; in perspective view and between top and side views, wind tunnel velocity vectors are shown

5.3 *Temporal* C_L *distribution throughout the wingbeat*

$C_L(\tau)$, for each species-speed combination, is determined from the $\bar{N}$ different spanwise downwash distributions using Eqs. 8 and 15 (Fig. 7). For both bat species, the majority of the lift is generated during the downstroke, while for $U_\infty = 4$ m/s and faster, negative lift ($C_L < 0$) is generated during part of the upstroke. Clear differences in the temporal lift distribution between the bat species can be distinguished. For *G. soricina*, lift increases rapidly at the

Table 2 *P*-values for the normalized lift estimate ($L/W-1$), the normalized induced power ($P_i\ (b/W)^2$), and the span efficiency e_i

	$L/W-1$		$P_i\ (b/W)^2$	$P_{i\ \text{ideal}}\ (b/W)^2$	e_i
	G. soricina	*L.yerbabuenae*			
Intercept	0.2016	**0.0092**	**0.0011**	**0.0012**	**<0.0001**
Species	–	–	0.0891	0.0674	**0.0295**
U_∞	0.1213	**0.0005**	–	–	0.7873
$U_\infty \times$ *species*	–	–	–	–	**0.0018**
$1/U_\infty$	–	–	**0.0001**	**0.0002**	–
$1/U_\infty \times$ *species*	–	–	0.3499	0.1608	–

The *P*-values in bold are significant

start of the downstroke, reaching a maximum peak around $\tau \approx 0.2$, whereafter C_L directly decreases. For *L. yerbabuenae*, C_L stays relatively constant at its maximum value throughout a large part of the downstroke ($\tau \in [0.2, 0.35]$), after which it decreases more rapidly.

5.4 Spanwise downwash distribution

The downwash distributions along the non-dimensional wake span ($y^* = y/b_w$) for different parts of the wingbeat (start of the downstroke, $\tau = 0$; mid downstroke, $\tau = 0.25$; end of the downstroke, $\tau = 0$, 50; mid upstroke, $\tau = 0.75$) are shown in Fig. 8, for both bat species, at $U_\infty = 2$, 4 and 7 m/s, respectively. For all flight speeds, the downwash is highest (most negative w) during mid downstroke, with its local spanwise maximum at the outer wing ($y^* = 0.4$). $w(y^*)$ decreases towards the inner wing and drops to zero behind the body. During the uptroke a clear upwash is present behind the outer wings at $U_\infty = 4$ and 7 m/s, while no upwash is observed at the lowest flight speed (2 m/s). The upwash behind the outer wings, resulting in negative lift, is primarily induced by the reversed vortex loops. Sometimes, an upwash is also present behind the body, notably for *L. yerbabuenae*.

Figure 9 shows the spanwise downwash distribution for all measured flight speeds, at mid downstroke ($\tau = 0.25$, Fig. 9a, b) and at mid upstroke ($\tau = 0.75$, Fig. 9c, d). At mid downstroke the downwash distribution is quite similar for all flight speeds, while at mid upstroke the downwash distribution varies much more with flight speeds. For the lowest flight speeds ($U_\infty < 3$ m/s) a downwash is present along the complete wingspan during the upstroke, while at the higher speeds ($U_\infty > 3$ m/s) an upwash is present behind the outer wing, where the reversed vortex loops are located. Also, especially for *L. yerbabuenae*, an upwash is present behind the body at multiple flight speeds, as previously noted.

5.5 Induced power and span efficiency

Using the modified actuator disk model the induced power for flapping flight was estimated (Fig. 6c and Table 2). Both the real and ideal normalized induced power $P_i(b/W)^2$ vary significantly with $1/U_\infty$, but not between species (Fig. 6c and Table 2). At the lowest speeds, P_i is lower than expected from Eq. 13, indicating relatively high flight efficiency at low flight speeds.

The average span efficiency throughout the measured flight speed range is estimated as $e_i = 0.81 \pm 0.03$ for *G. soricina* and $e_i = 0.79 \pm 0.03$ for *L. yerbabuenae* (see also Fig. 6d). e_i does vary significantly between the two bat species, but not with U_∞ (Table 2).

6 Discussion

A modified actuator disk model for forward flapping flight was constructed from time-resolved sequences of cross-stream PIV data from the near wake of two bat species flying freely in a wind tunnel over a speed range 2–7 m/s. Across this speed range, the mean calculated lift-to-weight ratio, L/W, for *G. soricina* does not differ from one ($L/W = 0.98 \pm 0.10$, Table 2), but for *L. yerbabuenae*, L/W is less than one ($L/W = 0.87 \pm 0.13$, Table 2), especially at the higher speeds (Fig. 6a). The fact that the induced downwash was measured in the near wake of the flying bats instead of at the wing, cannot explain the deficit in L/W for *L. yerbabuenae*, since this should rather result in an over-estimation of lift (Fig. 4a). For the actuator disk model developed here, streamwise induced velocities were ignored, since they could not be separated from wake defects due to drag. This probably results in an underestimation of the total mass flux (Eq. 6 and Fig. 2a). Since thrust forces can be assumed largest at the highest flight speeds (Muijres et al. 2011), and L/W is lowest at the highest flight speeds, one can assume that the underestimation of L/W is due to ignoring streamwise induced velocities.

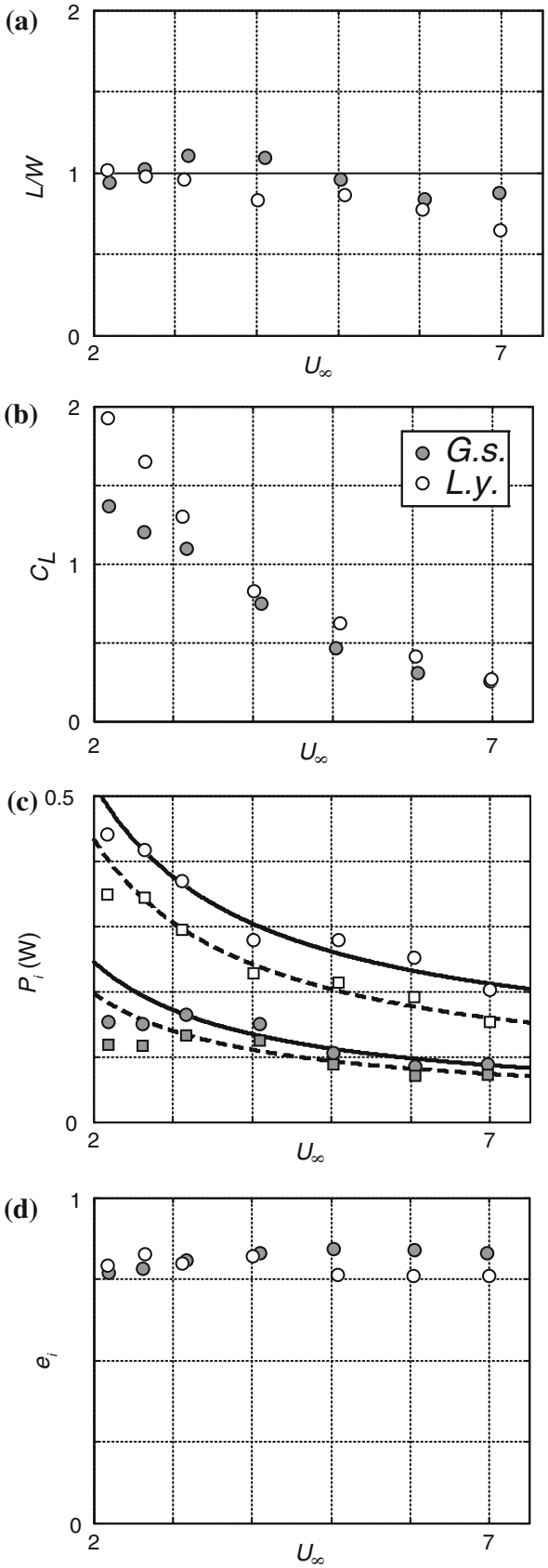

◀ **Fig. 6** Results from the actuator disk analysis for *G. soricina* (*filled symbols*) and *L. yerbabuenae* (*open symbols*) throughout the measured flight speed range. **a** The lift to weight ratio *L/W*. **b** the wingbeat average lift coefficient C_L. **c** datapoints and statistical trend lines of the real induced power P_i (*circle with solid line*) and ideal induced power $P_{i\,\mathrm{ideal}}$ (*square with dotted line*). **d** the span efficiency e_i

The wingbeat average C_L estimate (Fig. 6a) shows that the bats generated relatively high C_L values at low flight speeds ($C_L > 1$ at $U_\infty < 3$ m/s), which is high for steady state wings (Laitone 1997) but not uncommon for flapping wings (Hedenström and Spedding 2008; Muijres et al. 2008; Sane 2003).

The spanwise distribution of the vertical induced velocity behind the flying bats shows that these bats use the outer wing to generate the major part of the lift. The outer wing generates most lift because here, due to the flapping

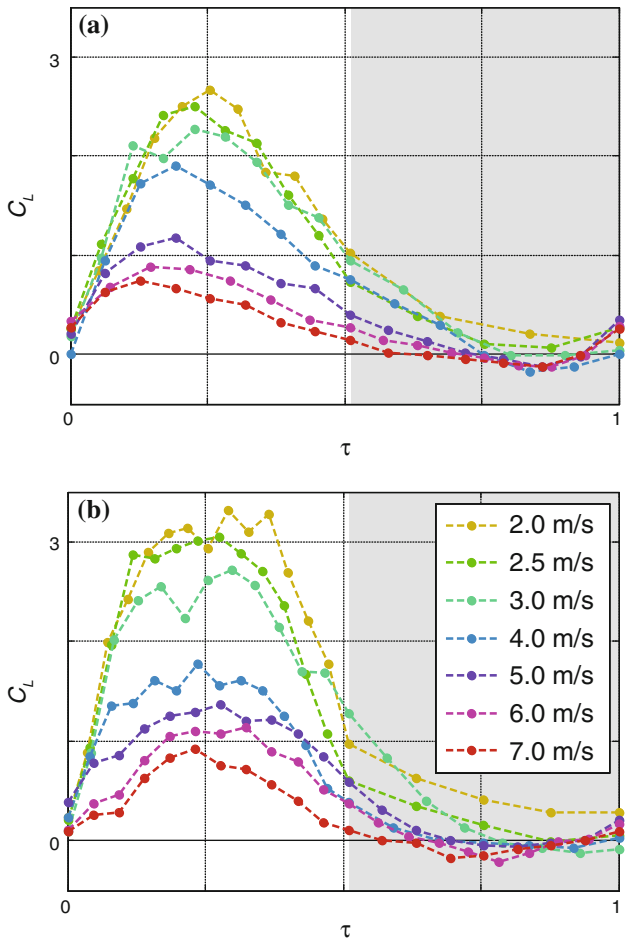

Fig. 7 The temporal C_L distributions throughout the wingbeat for different flight speeds, as indicated in the legend in panel (**b**). Panel (**a**) shows $C_L(\tau)$ for *G. soricina*, while panel (**b**) shows $C_L(\tau)$ for *L. yerbabuenae*. The grey area in both panels indicate upstroke

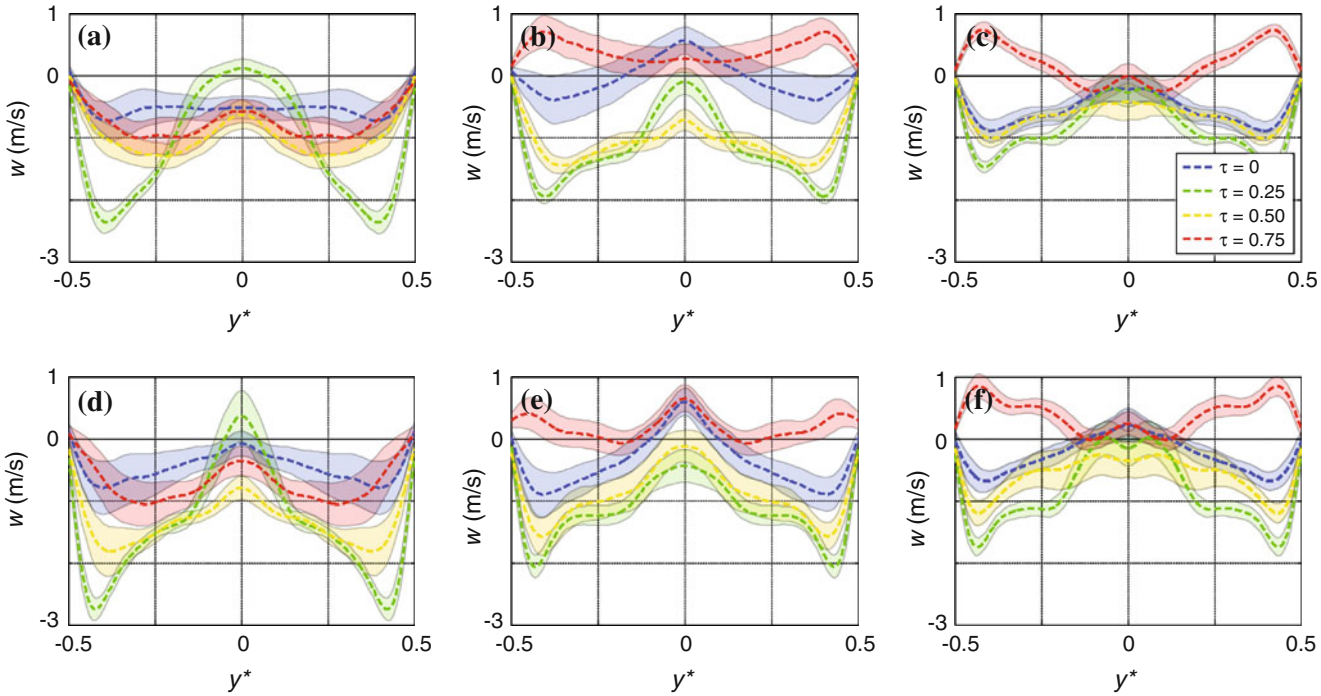

Fig. 8 Average spanwise downwash distributions $w(y^*)$, with 95% confidence interval, at different moments within the wingbeat. The top panels show data for *G. soricina* at 2 m/s (**a**), 4 m/s (**b**) and 7 m/s (**c**), while the bottom panels (**d**–**f**) show the equivalent data for *L. yerbabuenae*. Each panel shows the downwash at four points within the wingbeat: start of the downstroke ($\tau = 0$); mid downstroke ($\tau = 0.25$); end of the downstroke ($\tau = 0.5$); mid upstroke ($\tau = 0.75$), see legend in panel (**c**)

motion, both the angle-of-attack and the effective wing velocity are higher compared to the inner part of the wing (Wolf et al. 2010). Behind the body, induced velocity w is close to zero for large parts of the wingstroke, and even sometimes an upwash is present, resulting in negative lift generated by the body. This negative lift is probably generated by the wing membrane between the hind legs of the bats (*uropatagium*), and could be used for pitch control similar to the function of a horizontal tailplane in conventional airplanes. At the last part of the upstroke a "reversed vortex loop" is generated by each wing (Fig. 5), which also results in negative lift.

There are multiple hypotheses for explaining the presence of the reversed vortex loops. Reversed vortex loops could be generated due to limitations in the membranous wing morphology and wing kinematics (Hedenström et al. 2007), and/or could be used for maneuverability and stability control (Johansson et al. 2008), or the reversed vortex loops could be used for thrust generation with negative lift as a by-product (Muijres et al. 2011). The pattern of the induced velocities as a result of the reversed vortex loops is strikingly similar to the wake pattern at the equivalent part of the wingbeat and wing section of an optimal flapping wing with a relatively high thrust requirement (lift-to-drag ratio $L/D = 5$, Hall et al. 1998, similar to the L/D values estimated for these bats, Muijres et al. 2011). The optimum is the wingbeat kinematics with the lowest power requirement for the prescribed lift and thrust production. For $L/D = 5$, the optimal flapping wing generates thrust in combination with negative lift at the outer part of the wing during the upstroke (Hall et al. 1998). Since one can assume that thrust requirements increase with increasing flight speed, and the upwash at the reversed vortex loop for the bats also increase with flight speed, the results support the last hypothesis for explaining the presence of the reversed vortex loops.

When controlling for span loading, the induced power estimate did not differ significantly between the two bat species (Table 2). At the lowest flight speeds the induced power, P_i, was lower than expected from Eq. 13 (Fig. 6c). This can be explained by the fact that at the lowest flight speeds the difference between U_∞ and $U_{\infty,\,\mathrm{eff}}$ is largest. e.g. at $U_\infty = 2$ m/s the wings operate effectively at an average speed of $U_{\infty,\,\mathrm{eff}} = 3.26$ m/s. Indirect support for this result comes from respirometry measurements of flying *G. soricina*, where metabolic rate of hovering was similar to that of forward flight (Winter 1998).

Norberg et al. (1993) used an ideal actuator disk model in combination with hot-wire anemometry measurements to estimate the induced power and span efficiency for *G. soricina* during hovering flight. Our induced power estimate for *G. soricina* at a speed of 2 m/s ($P_i = 0.153$ W) is

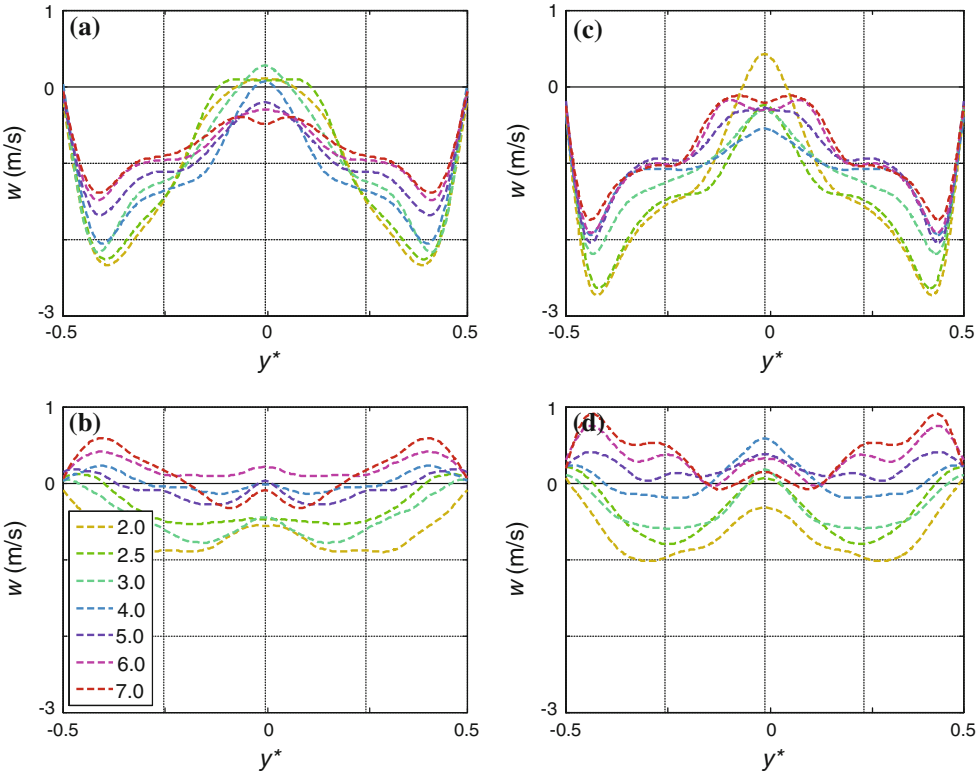

Fig. 9 Average spanwise downwash distributions $w(y^*)$ for the complete measured flight speed range. **a** Downwash at mid downstroke ($\tau = 0.25$) for *G. soricina*. **b** Downwash at mid upstroke ($\tau = 0.75$) for *G. soricina*. **c** Downwash at mid downstroke ($\tau = 0.25$) for *L. yerbabuenae*. **d** Downwash at mid upstroke ($\tau = 0.75$) for *L. yerbabuenae*. The different speeds are color coded as shown in panel (**b**)

similar to their estimate for hovering flight ($P_i = 0.147$ W), while our ideal power estimate ($P_{i\ \text{ideal}} = 0.118$ W) is higher than $P_{i\ \text{ideal}} = 0.094$ W estimated by Norberg et al. (1993). This difference in $P_{i\ \text{ideal}}$ results in a higher span efficiency estimated here for *G. soricina* at 2 m/s ($e_i = 0.77$) than $e_i = 0.64$ estimated by Norberg et al. (1993). The difference in ideal induced power can be explained by the fact that in the present study, the ideal induced power presumes only a spanwise uniform downwash at each time step (Eqs. 9–11), instead of a uniform downwash throughout the complete wingbeat as assumed in Norberg et al. (1993). Since e_i is defined as the factor describing the deviation from a uniform spanwise downwash (Spedding and McArthur 2010), we would argue that assuming a spanwise uniform downwash distribution for the $P_{i\ \text{ideal}}$ calculation results in a better estimate for the true span efficiency.

The average estimations of the span efficiency throughout the flight speeds range for both bat species ($e_i = 0.81 \pm 0.03$ for *G. soricina* and $e_i = 0.79 \pm 0.03$ for *L. yerbabuenae*), are somewhat lower than estimates from other animal flight studies (gliding kestrel, $e_i = 0.96$, Spedding 1987; desert locust at mid downstroke, $e_i = 0.85$ to 0.89, Bomphrey et al. 2006), similar to values assumed in bird flight models ($e_i = 0.83$, Pennycuick 2008b), but high compared to the highest estimate of e_i for a steady Eppler 387 wing at similar *Re* ($e_i = 0.76$, Spedding and McArthur 2010). The fact that gliding kestrels have higher e_i could mean that birds have inherently higher span efficiency, but also that gliding flight results in higher e_i than flapping flight, although the results by Spedding and McArthur (2010) indicate the opposite. The span efficiency for the desert locust was estimated using a similar technique as that used here (Bomphrey et al. 2006). However, the span efficiency was estimated at mid downstroke only, while the span efficiencies reported here are the average e_i for the whole wingbeat. We have estimated e_i at mid downstroke at 0.79 ± 0.06 for *G. soricina* and 0.79 ± 0.04 for *L. yerbabuenae*, suggesting that desert locusts would have higher e_i than bats, at least at mid downstroke. This difference may be a consequence of the relatively low downwash behind the body of bats as a result of low body lift and creating an unfavorable spanwise downwash distribution (Fig. 9a, b).

The above comparison shows that bat flight has relatively low span efficiency compared to other flying animals, possibly due to relatively low body lift in bats. But, since this is the first empirical estimate of the span efficiency throughout a complete wingbeat, we cannot conclusively distinguish relative flight efficiency of bat compared to birds and insects from general flapping flight efficiency compared to steady wings. Therefore, a future comparison with similar data from birds, insects, and mechanical flappers would be very informative.

In conclusion, we show here how the modified actuator disk model together with high-speed PIV data can be used

to obtained high-resolution temporal and spanwise downwash distribution of flapping flight. The method works without the need to model or measure complex wing-wake interactions. By applying this approach, we can derive key aerodynamic properties of flapping flight such as the temporal lift distribution, the induced power, and the span efficiency. The induced power and the span efficiency for *G. soricina* at the lowest flight speed are similar to that of previous estimates for a hovering *G. soricina* (Norberg et al. 1993).

Acknowledgments We would like to thank Rhea von Busse for her extensive help during the experiments, and Christoffer Johansson for his advice concerning the analysis. The Lavision stereo PIV system was acquired through a generous grant from the Knut and Alice Wallenberg foundation. The research was funded by the Swedish Research Council to A.H. This report received support from the Center for Animal Movement Research (CAnMove) financed by a Linnaeus grant (349-2007-8690) from the Swedish Research Council and Lund University.

References

Anderson JD (1991) Fundamentals of aerodynamics. McGraw Hill, New York

Bomphrey RJ, Taylor GK, Lawson NJ, Thomas AL (2006) Digital particle image velocimetry measurements of the downwash distribution of a desert locust Schistocerca gregaria. J Roy Soc Interface 3(7):311–317

Ellington CP (1984) The aerodynamics of hovering insect flight. V. A vortex theory. Philos Trans R Soc B-Biol Sci 305(1122): 115–144

Gessow A, Myers GC (1952) Aerodynamics of the helicopter. Frederick Ungar Publishing Co, New York

Grundy TM, Keefe GP, Lowson MV (2001) 'Effects of acoustic disturbances on Low Re Aerofoil flows. Fixed Flapping Wing Aerodynamics for Micro Air Vehicle Applications 195:91–112

Hall KC, Hall SR (1996) Minimum induced power requirements for flapping flight. J Fluid Mech Digit Arch 323(-1):285–315

Hall KC, Pigott SA, Hall SR (1998) Power requirements for large-amplitude flapping flight. J Aircr 35(3):352–361

Hedenström A, Spedding G (2008) Beyond robins: aerodynamic analyses of animal flight. J Roy Soc Interface 5(23):595–601

Hedenström A, Rosén M, Spedding GR (2006) Vortex wakes generated by robins Erithacus rubecula during free flight in a wind tunnel. J Roy Soc Interface 3(7):263–276

Hedenström A, Johansson L, Wolf M, von Busse R, Winter Y, Spedding G (2007) Bat flight generates complex aerodynamic tracks. Science 316(5826):894–897

Hedenström A, Muijres F, von Busse R, Johansson L, Winter Y, Spedding G (2009) High-speed stereo DPIV measurement of wakes of two bat species flying freely in a wind tunnel. Exp Fluids 46(5):923–932

Henningsson P, Muijres FT, Hedenström A (2010) Time-resolved vortex wake of a common swift flying over a range of flight speeds. J Roy Soc Interface. doi:10.1098/rsif.2010.0533

Hubel T, Hristov N, Swartz S, Breuer K (2009) Time-resolved wake structure and kinematics of bat flight. Exp Fluids 46(5):933–943

Hubel TY, Riskin DK, Swartz SM, Breuer KS (2010) Wake structure and wing kinematics: the flight of the lesser dog-faced fruit bat, Cynopterus brachyotis. J Exp Biol 213(20):3427–3440

Johansson LC, Hedenström A (2009) The vortex wake of blackcaps (Sylvia atricapilla L.) measured using high-speed digital particle image velocimetry (DPIV). J Exp Biol 212(20):3365–3376

Johansson LC, Wolf M, von Busse R, Winter Y, Spedding GR, Hedenström A (2008) The near and far wake of Pallas' long tongued bat (Glossophaga soricina). J Exp Biol 211(18):2909–2918

Laitone E (1997) Wind tunnel tests of wings at Reynolds numbers below 70, 000. Exp Fluids 23(5):405

Lentink D, Gerritsma M (2003) Influence of airfoil shape on performance in insect flight. In: Proceedings of 33rd AIAA fluid dynamics conference and exhibit

Lissaman P (1983) Low-Reynolds-Number airfoils. Ann Rev Fluid Mech 15(1):223–239

Muijres F, Johansson L, Barfield R, Wolf M, Spedding G, Hedenström A (2008) Leading-Edge Vortex improves lift in Slow-Flying Bats. Science 319(5867):1250–1253

Muijres FT, Johansson LC, Winter Y, Hedenström A (2011) Comparative aerodynamic performance of flapping flight in two bat species using time-resolved wake visualization. J Roy Soc Interface. doi:10.1098/rsif.2011.0015

Norberg UM, Rayner JMV (1987) Ecological morphology and flight in bats (mammalia; chiroptera): wing adaptations, flight performance, foraging strategy and echolocation. Philos Trans Roy Soc Lond B Biol Sci 316(1179):335–427

Norberg U, Kunz T, Steffensen J, Winter Y, von Helversen O (1993) The cost of hovering and forward flight in a nectar-feeding bat, Glossophaga soricina, estimated from aerodynamic theory. J Exp Biol 182(1):207–227

Pennycuick C (1968) Power requirements for horizontal flight in the pigeon Columba Livia. J Exp Biol 49(3):527–555

Pennycuick CJ (1971) Gliding flight of the dog-faced bat rousettus aegyptiacus observed in a wind tunnel. J Exp Biol 55(3): 833–845

Pennycuick CJ (1973) Wing profile shape in a fruit-bat gliding in a wind tunnel, determined by photogrammetry. Periodicum Biologorum 75:77–82

Pennycuick C (2008a) Chapter 6 the membrane wings of Bats and Pterosaurs. In: Proceedings of modelling the flying bird, vol 5. Academic Press, New York, pp 135–160

Pennycuick CJ (2008b) Modelling the flying bird. Elsevier, Amsterdam

Pennycuick C, Alerstam T, Hedenström A (1997) A new low-turbulence wind tunnel for bird flight experiments at Lund University, Sweden. J Exp Biol 200(10):1441–1449

Pesavento U, Wang ZJ (2009) Flapping wing flight can save aerodynamic power compared to steady flight. Phys Rev Lett 103(11):118102

Rosén M, Spedding G, Hedenström A (2007) Wake structure and wingbeat kinematics of a house-martin *Delichon urbica*. J Roy Soc Interface 4(15):659–668

Sane S (2003) The aerodynamics of insect flight. J Exp Biol 206(23):4191–4208

Spalart PR (2003) On the simple actuator disk. J Fluid Mech 494(-1): 399–405

Spedding GR (1987) The Wake of a Kestrel (Falco Tinnunculus) in Gliding Flight. J Exp Biol 127(1):45–57

Spedding G, Hedenström A (2009) PIV-based investigations of animal flight. Exp Fluids 46(5):749–763

Spedding GR, McArthur J (2010) Span efficiencies of wings at low Reynolds Numbers. J Aircr 47(1):120–128

Spedding GR, Rosen M, Hedenström A (2003a) A family of vortex wakes generated by a thrush nightingale in free flight in a wind tunnel over its entire natural range of flight speeds. J Exp Biol 206(14):2313–2344

Spedding GR, Hedenström A, Rosen M (2003b) Quantitative studies of the wakes of freely flying birds in a low-turbulence wind tunnel. Exp Fluids 34(2):291–303

Spedding GR, Hedenström AH, McArthur J, Rosen M (2008) The implications of low-speed fixed-wing aerofoil measurements on the analysis and performance of flapping bird wings. J Exp Biol 211(2):215–223

Stepniewski WZ, Keys CN (1984) Rotary-wing aerodynamics. Courier Dover Publications, New York

Swartz SM, Groves MS, Kim HD, Walsh WR (1996) Mechanical properties of bat wing membrane skin. J Zool 239(2):357–378

Swartz SM, Iriarte-Diaz J, Riskin DK, Song A, Tian X, Willis DJ, Breuer KS (2007). Wing structure and the aerodynamic basis of flight in bats. In: Proceedings of AIAA aerospace science meeting, vol 42

Wang ZJ (2008) Aerodynamic efficiency of flapping flight: analysis of a two-stroke model. J Exp Biol 211(2):234–238

Winter Y (1998) Energetic cost of hovering flight in a nectar-feeding bat measured with fast-response respirometry. J Comp Physiol 168(6):434–444

Wolf M, Johansson LC, von Busse R, Winter Y, Hedenström A (2010) Kinematics of flight and the relationship to the vortex wake of a Pallas' long tongued bat (Glossophaga soricina). J Exp Biol 213(12):2142–2153